Available online at www.sciencedirect.com

ScienceDirect

journal homepage: www.elsevier.com/locate/he

Core-shell Ni_3Fe-based nanocomposites for the oxygen evolution reaction

Xue Bai [a], *Yuanyuan Ma* [b], *Qiang Wang* [a], *Jingqi Guan* [a,*]

[a] *Institute of Physical Chemistry, College of Chemistry, Jilin University, 2519 Jiefang Road, Changchun, 130021, PR China*

[b] *College of Chemistry and Chemical Engineering, Qiqihar University, Qiqihar, 161006, China*

HIGHLIGHTS

- Core-shell $Ni_3Fe_1O_x$@C catalysts are fabricated by an annealing method.
- $Ni_3Fe_1O_x$@C-800 exhibits an overpotential of only 264 mV at 10 mA cm^{-2}.
- Bimetallic $Ni_3Fe_1O_x$@C-800 show lower OER barrier than monometallic counterpart.
- The charge transfer ability can be enhanced by the core-shell structure.
- The large ECSA of $Ni_3Fe_1O_x$@C-800 favors exposing more active sites.

GRAPHICAL ABSTRACT

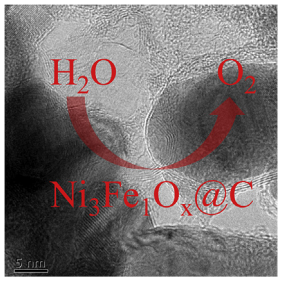

ARTICLE INFO

Article history:
Received 13 August 2021
Received in revised form
26 August 2021
Accepted 17 October 2021
Available online 3 November 2021

Keywords:
Energy barrier
Iron
Nickel
Oxygen evolution reaction
Tartaric acid

ABSTRACT

To deal with energy and environmental issues, it is necessary to exploit efficient and stable electrocatalysts for the generation of clean hydrogen. Herein, we describe the synthesis of bimetallic Fe/Ni alloy encapsulated by amorphous carbon shells via a facile annealing strategy for electrocatalytic oxygen evolution reaction (OER). The ferric nickel tartrate annealed at 800 °C ($Ni_3Fe_1O_x$@C-800) exhibits a low OER overpotential of 264 mV at 10 mA cm^{-2} and good stability in alkaline media. Compared with monometallic counterpart, bimetallic Ni_3Fe-based nanocomposites show lower OER barrier (ca. 324 kJ mol^{-1}) due to a cooperation mechanism between Ni and Fe sites in promoting electrocatalytic water oxidation. Compared with those annealed at other temperatures, the enhanced OER performance of $Ni_3Fe_1O_x$@C-800 can be ascribed to the large electrochemical surface area for exposing more active sites, smaller charge transfer, and better intrinsic activity of Ni_3Fe-based sites.

* *Corresponding author.*
E-mail address: guanjq@jlu.edu.cn (J. Guan).

https://doi.org/10.1016/j.ijhydene.2021.10.119

Introduction

The electrolysis of water for generating hydrogen via renewable energy sources is an efficient carbon-neutral technology for clean energy production [1–5]. However, the large-scale implement of brine electrolysis is seriously restricted by the scarcity of noble metal Ir-/Ru-based catalysts for facilitating the sluggish anodic oxygen evolution reaction (OER) [6–9]. Ni-based catalysts with unique structural and chemical properties are regarded as the most potential alternatives to the precious Ir-based catalysts for the OER in alkaline electrolytes [10–13]. Especially, nanostructured Ni alloys with modified electronic structures are outstanding OER electrocatalysts in alkaline media [14,15]. Thereinto, NiFe-based oxides/(oxy)hydroxides have been extensively investigated as one of the most high-efficiency OER electrocatalysts owing to a cooperative mechanism between Ni and Fe sites [16,17]. Lin et al. found that the Ni–Fe hydroxide would be deactivated after the dissociation of Fe and formation of the FeOOH secondary phase [17]. Hu et al. found that the Fe sites had higher OER activity than the Ni sites in NiFe layered double hydroxide with an Fe content of 4.7% [18]. Since the active species in the catalyst could greatly influence the electrochemical property, the rational fabrication of nanostructures for NiFe-based catalysts by increasing the intrinsic active centers is the key to enhance the OER activity [19].

To enhance the electrocatalytic activity of NiFe-based nanocomposite catalysts, different strategies have been developed, including size and morphology control [20,21], supporting them on high specific area substrates [22,23], metal doping (e.g. Co [24], Al [25], Cd [26], Cu [27], Mo [28], and Ir [29]), nonmetal doping (e.g. N [30], P, B, S [31], and Se [32]), defect engineering [33], and lattice strain [34]. For size and morphology control, nanoparticles, nanosheets, porous structures, and core-shell structures have been successfully fabricated [35]. Thereinto, using carbon shells to encapsulate active NiFe alloys is an effective method to avoid the direct contact with electrolytes and protect them from oxidation. For instance, Wang and co-workers wrapped N-doped graphitic shell around the NiFe alloy for the OER with an overpotential of 320 mV at 10 mA cm^{-2} in alkaline media [36]. Bao et al. coated a NiFe alloy with N-doped carbon shells, which demonstrated an overpotential of 280 mV at 10 mA cm^{-2} in alkaline media [37]. Gong et al. found that Ni_3Fe alloys incorporated in N-doped carbon exhibited an overpotential of 330 mV at 10 mA cm^{-2} [38]. Xie et al. reported Ni_3Fe alloys embedded into boron-doped carbon displayed an overpotential of 280 mV at 10 mA cm^{-2} [39]. By theoretical calculations, Zhao et al. revealed that 1/4 monolayer O covered

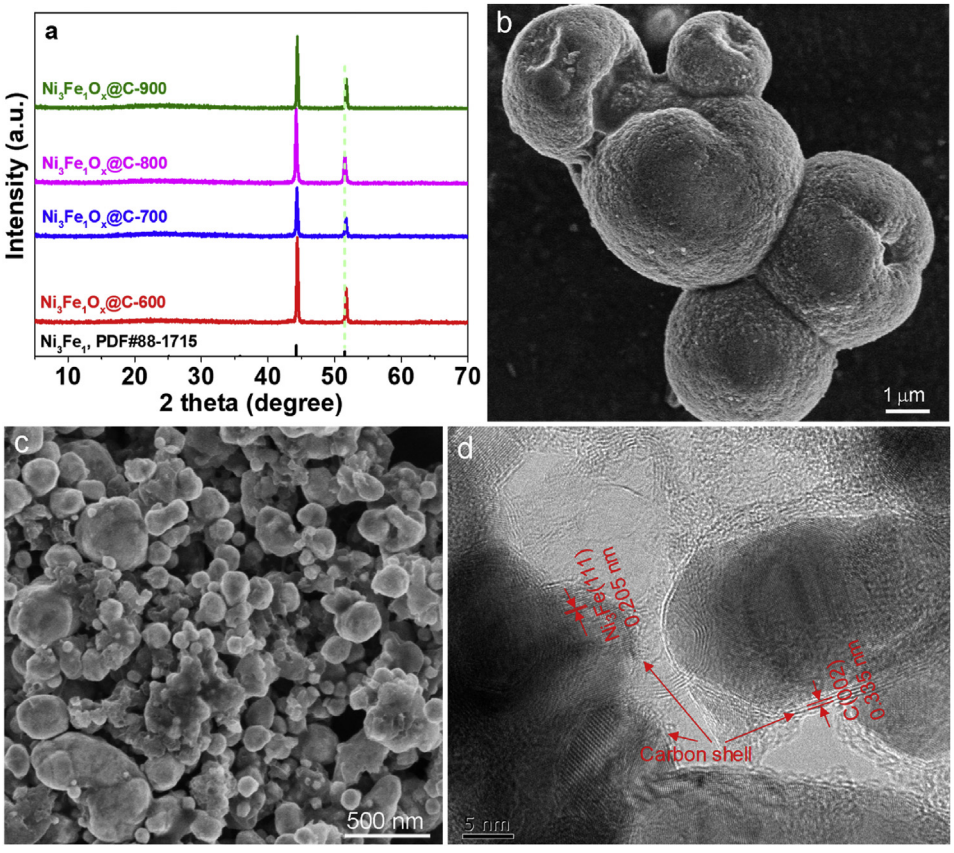

Fig. 1 – (a) XRD patterns of $Ni_3Fe_1O_x$@C-T and referred sample Ni_3Fe_1. (b) SEM image of Ni_3Fe_1-TA. (c) SEM image of $Ni_3Fe_1O_x$@C-800. (d) HRTEM image of $Ni_3Fe_1O_x$@C-800.

surface in Ni_3Fe-layered double hydroxides combined with the OH readily [40]. However, until now, there are still no efficient methods to adjust the proportion of the coated bimetals, which results in difficulty to correlate the active species and OER performance.

In this work, we report a facile annealing method to encapsulate a Ni_3Fe alloy within ultrathin amorphous carbon layers. By modulating the annealing temperature and the Ni/Fe proportion, the active species and electron structure of the as-synthesized catalyst can be efficiently optimized, promoting the OER process. The optimized catalyst annealed at 800 °C with a Ni/Fe ratio of 3/1 showed better OER activity and stability than commercial IrO_2 electrocatalyst.

Experimental section

Materials preparation

Synthesis of Ni_nFe_1-TA

Ferric nickel tartrate (Ni_nFe_1-TA) was solvothermally synthesized. In a typical synthesis, 178 mg $NiCl_2 \cdot 6H_2O$, 67 mg $FeCl_3 \cdot 6H_2O$, and 300 mg tartaric acid were dissolved in 40 mL N, N-dimethylformamide, which was transferred into 50 mL Teflon autoclave and heated at 110 °C for 24 h. The obtained green solid was denoted as Ni_3Fe_1-TA. For comparison, Fe-TA, Ni-TA, and Ni_nFe_1-TA with different Ni/Fe ratios were synthesized by a similar solvothermal synthesis method.

Synthesis of $Ni_nFe_1O_x$@C-T

The obtained Ni_nFe_1-TA was annealed under the protection of nitrogen at different temperatures for 2 h, which was nominated as $Ni_nFe_1O_x$@C-T (T = 600, 700, 800, and 900 °C). For comparison, FeO_x@C-800 and NiO_x@C-800 were also synthesized by annealing Fe-TA and Ni-TA, respectively.

Characterization

The phase of the catalysts was identified by XRD with Cu Kα radiation (λ = 1.5418 Å). Scanning electron microscope (SEM) images were taken on a HITACHI SU8020 operated at 30 kV. High resolution transmission electron microscopy (HRTEM) was conducted on a FEI Tecnai F20 microscope operated at an

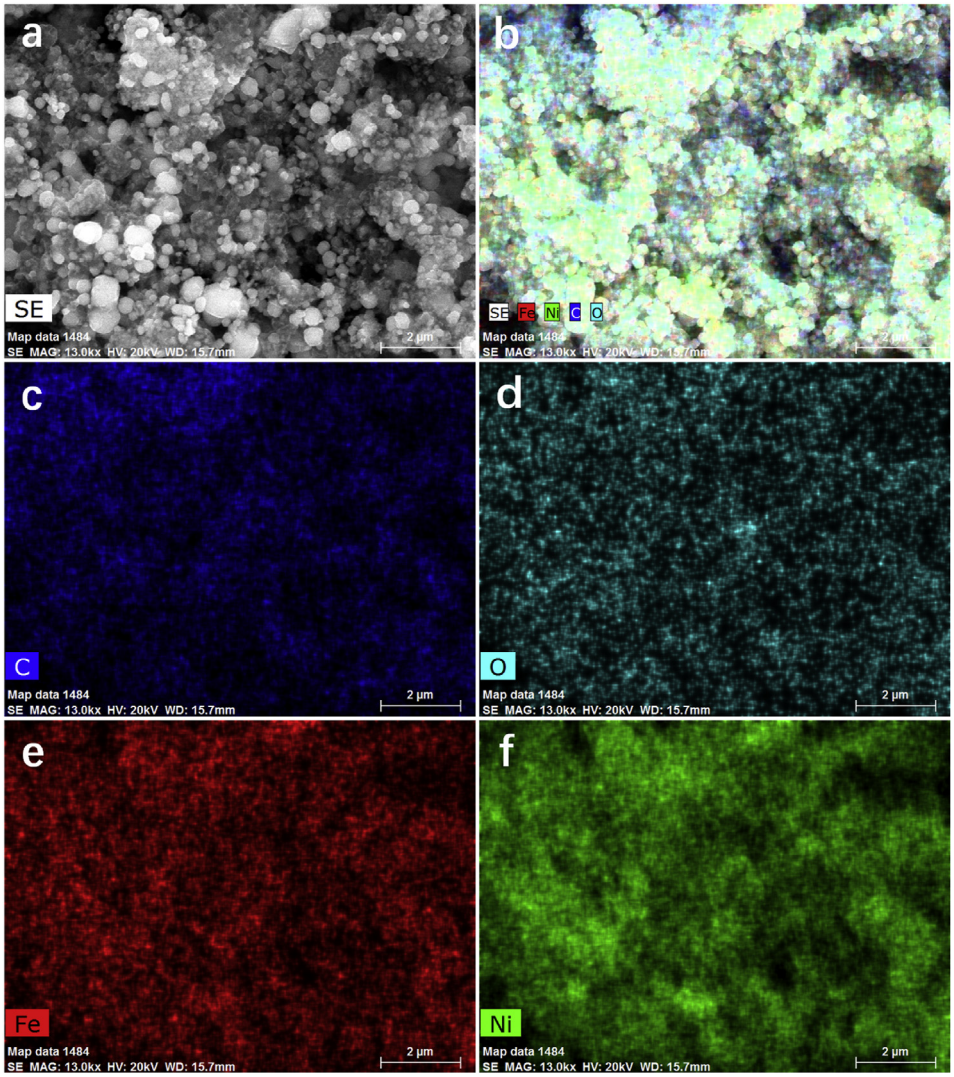

Fig. 2 – (a) SEM image of $Ni_3Fe_1O_x$@C-800, and (b–f) the corresponding EDS mapping of C, O, Fe, and Ni.

accelerating voltage of 200 kV. The XPS analysis was carried out on a Thermo ESCALAB 250Xi. The C 1s peak position was selected at 284.6 eV.

Electrochemical measurements

Electrochemical measurements were performed a three-electrode system (CHI. 760E). The as-synthesized samples, saturated calomel electrode (SCE), and Pt were used as the working electrode, reference electrode, and counter electrode, respectively. In all measurements, the SCE was calibrated with respect to RHE according to the formula: E (RHE) = E (SCE) + 0.241 + 0.0591 pH. LSV curves were conducted with 90% iR-compensation. The EIS measurements were investigated in the frequency from 100 kHz to 0.1 Hz.

Results and discussion

The successful fabrication of Ni_nFe_1-TA was demonstrated by powder X-ray diffraction (XRD). As exhibited in Fig. S1, the intensity of diffraction peaks becomes weak gradually when the Ni/Fe ratio increase, indicating that a bimetallic tartrate was successfully synthesized. After annealing, the Ni_nFe_1-TA was decomposed and metallic iron/nickel and their alloy surrounded by amorphous carbon was formed. As displayed in Fig. 1a and Fig. S2, the $Ni_3Fe_1O_x$@C-800 shows two strong XRD peaks at 44.2 and 51.5°, attributable to the Ni_3Fe nanoparticles. Moreover, the $Ni_3Fe_1O_x$@C annealed at 600, 700, and 900 °C exhibit a mixed structure of metallic Fe, Ni, and Ni_3Fe, suggesting that the annealing temperature has great influence on the structure of Ni_3Fe_1-TA-derived materials.

The SEM images show that the nanoparticles in the $Ni_3Fe_1O_x$@C-800 are spherical morphology, which is similar to the parent Ni_3Fe_1-TA (Fig. 1b and c). The structure of $Ni_3Fe_1O_x$@C-800 was further identified by HRTEM. As illustrated in Fig. 1d, the nanoparticles were wrapped by ultrathin amorphous carbon shells (<1 nm). The interplanar spacing in the nanoparticles is 0.205 nm, corresponding to the (111) crystal plane of the Ni_3Fe alloy in good agreement with the XRD results. The element distribution in the $Ni_3Fe_1O_x$@C-800 was analyzed by SEM-EDS. AS revealed in Fig. 2, the Fe and Ni elements are uniformly dispersed in the $Ni_3Fe_1O_x$@C-800 sample.

The XPS survey spectrum of $Ni_3Fe_1O_x$@C-800 reveals the presence of carbon, nickel, iron, and oxygen species (Fig. 3a). The corresponding high-resolution XPS Fe $2p_{3/2}$ spectrum of $Ni_3Fe_1O_x$@C-800 can be deconvoluted into Fe^0 (707.3 eV), Fe^{2+} (710.9 eV), and Fe^{3+} (713.1 eV) (Fig. 3b) [41–45]. The high-resolution XPS spectrum of Ni $2p_{3/2}$ can be convoluted into two peaks centered at 852.8 and 855.9 eV, corresponding to Ni^0 and Ni^{2+}, respectively (Fig. 3c) [46,47]. The high-resolution XPS spectrum of O 1s can be fitted into two peaks located at 530.5 and 533.4 eV, ascribed to M − O (M = Fe and Ni) and defective oxygen sites, respectively (Fig. 3d) [21,45,48,49].

The OER activity of the as-prepared samples was investigated by the polarization curves at a scan rate of 5 mV s^{-1} with the iR-compensation in 1.0 M KOH using a typical three-electrode equipment. As shown in Fig. S3, the NiO_x@C-800 annealed at 800 °C presents the best OER activity with the lowest overpotential at 10 mA cm^{-2} (η_{10}), while either the

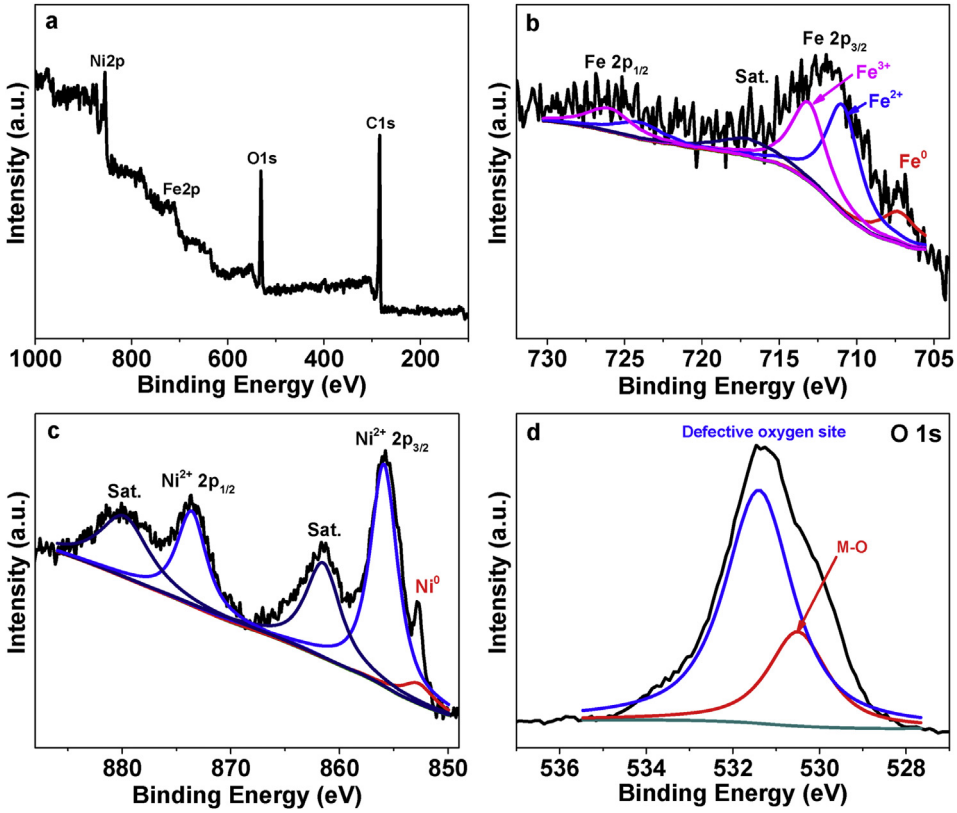

Fig. 3 – XPS survey spectrum (a), and high-resolution XPS spectra of Fe 2p (b), Ni 2p (c), and O 1s (d) of the $Ni_3Fe_1O_x$@C-800.

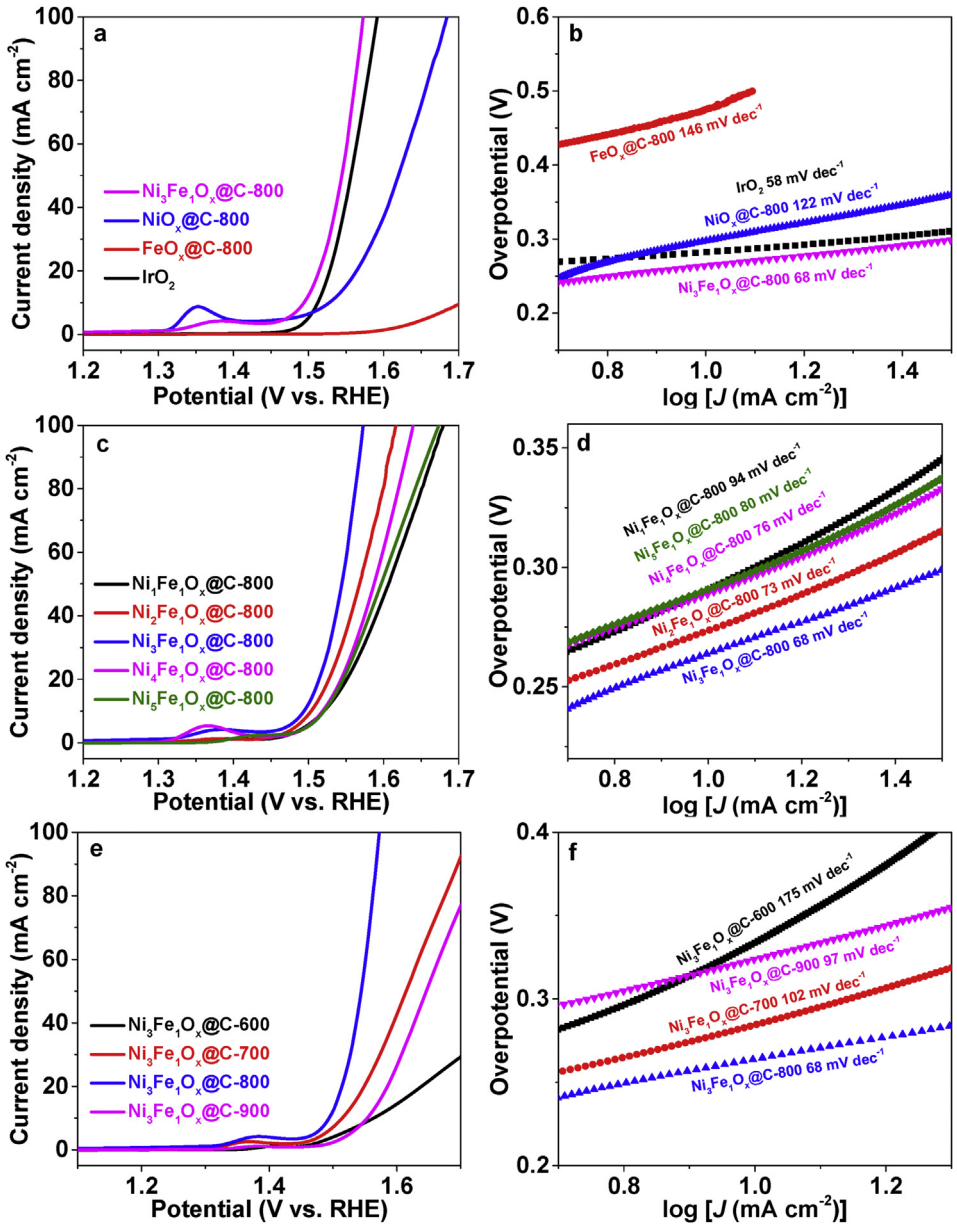

Fig. 4 – (a) LSV curves of IrO_2, FeO_x@C-800, NiO_x@C-800, and $Ni_3Fe_1O_x$@C-800. (b) Tafel plots. (c) LSV curves of $Ni_nFe_1O_x$@C-800. (b) Tafel plots. (e) LSV curves of $Ni_3Fe_1O_x$@C-T. (f) Tafel plots.

higher or lower annealing temperatures result in the decreased OER activity. From XRD patterns, with increasing the annealing temperature, the relative content of NiO/Ni species increases (Fig. S4). Thus, the annealing temperature of 800 °C is perceived as the representative one for exploring the Fe-doping effects on its OER performance. Thereby, the OER activity of FeO_x@C-800, NiO_x@C-800, and $Ni_3Fe_1O_x$@C-800 are further compared (Fig. 4a). The FeO_x@C-800 shows a high overpotential (η_{10}) of 475 mV, indicating its poor OER property. Both NiO_x@C-800 and $Ni_3Fe_1O_x$@C-800 show prominent OER activity with a rapid raise of electrocatalytic current at high overpotentials. Introduction of Fe further decreases the η_{10} from 298 mV of NiO_x@C-800 to 264 mV, even lower than that of commercial IrO_2 (282 mV). The derived Tafel slope of $Ni_3Fe_1O_x$@C-800 is 68 mV dec^{-1}, smaller than those of FeO_x@C-800 (146 mV dec^{-1}) and NiO_x@C-800 (122 mV dec^{-1}), indicating more favorable OER kinetics on the former (Fig. 4b). The OER activity of $Ni_3Fe_1O_x$@C-800 is comparable to or even better than those of the state-of-the-art Fe/Ni-based OER electrocatalysts in alkali (Table 1). The OER energy barrier (ΔG) on the $Ni_3Fe_1O_x$@C-800 was calculated using following formula (1-3) [50].

$$j = j_0 * \left[-e^{\frac{-\alpha nF(E-E_0)}{RT}} + e^{\frac{(1-\alpha)nF(E-E_0)}{RT}} \right] \quad (1)$$

$$\Delta G = (1-\alpha)nFE_0 - (1-\alpha)nFE \quad (2)$$

$$1-\alpha = \frac{1}{1+\frac{-a_1}{a_2}} \quad (3)$$

Table 1 – OER performance on various catalysts.

Catalyst	Electrolyte	η_{10} (mV)	Tafel slope (mV dec^{-1})	Ref.
$Ni_3Fe_1O_x$@C-800	1.0 M KOH	264	68	This work
NiFe@CN-G	1.0 M KOH	320	41	[36]
FeNi@Gr	1.0 M KOH	280	70	[37]
Porous Ni_2P	1.0 M KOH	320	105	[51]
Fe_2O_3@Ni-MOF-74	1.0 M KOH	264	48	[52]
Fe_1Ni_2-BDC	1.0 M KOH	260	35	[53]
NFN-MOF/NF	1.0 M KOH	240	58.8	[54]
$Fe_{0.75}Ni_{0.25}S_2$	1.0 M KOH	247	47.6	[55]
Ni-MOF@Fe-MOF	1.0 M KOH	265	82	[56]
$NiFe_x$@$NiFe_2O_4$@NC	1.0 M KOH	262	51.4	[57]
NiO/C@NiFe-LDHs	1.0 M KOH	299	45	[58]
DR-Ni_3FeN/NG	1.0 M KOH	250	38	[59]
$Co_{2.36}Fe_{0.19}Ni_{0.45}$-btca	1.0 M KOH	292	72.6	[60]
$CoNi_{0.2}Fe_{0.05}$-ZHP	1.0 M NaOH	329	48.2	[61]

where T is the test temperature, R is the gas constant, n is the electron transfer number, F is the Faraday constant, J_0 is the exchange current density, a is the Tafel slope. The ΔG is calculated to be ca. 324 kJ mol^{-1} for $Ni_3Fe_1O_x$@C-800, far smaller than those of FeO_x@C-800 (392 kJ mol^{-1}) and NiO_x@C-800 (358 kJ mol^{-1}), suggesting that Fe-doped Ni-based catalysts can efficiently reduce OER energy barrier.

The influence of Ni/Fe ratio on the OER activity was studied. As demonstrated in Fig. 4c, the OER activity increases initially with raising the Ni/Fe ratio and reaches a maximum at Ni/Fe = 3/1. Further increasing the Ni/Fe ratio leads to decreased activity, suggesting that appropriate Ni/Fe ratio favors the formation of highly active sites for the OER. The smaller Tafel slope of $Ni_3Fe_1O_x$@C-800 than other $Ni_nFe_1O_x$@C-800 further implies that appropriate Ni/Fe ratio can facilitate the OER electrocatalysis due to a cooperative mechanism between Ni and Fe sites (Fig. 4d) [18,62]. Then, the influence of annealing temperature on the electrocatalytic OER performance of $Ni_3Fe_1O_x$@C was investigated. As exhibited in Fig. 4e and f, like Fe-free samples, Ni_3Fe_1-TA annealing at 800 °C shows the highest OER activity and the smallest Tafel slope. From the aforementioned XRD analysis, we know that $Ni_3Fe_1O_x$@C-800 possesses a main species of Ni_3Fe alloy, while $Ni_3Fe_1O_x$@C-600, $Ni_3Fe_1O_x$@C-700 and $Ni_3Fe_1O_x$@C-900 all show a mixed species of metallic Fe, Ni, and Ni_3Fe. In addition, $Ni_1Fe_1O_x$@C-800 and $Ni_2Fe_1O_x$@C-800 show a mixed species of metallic Fe and Ni_3Fe, while $Ni_4Fe_1O_x$@C-800 exhibits a mixed species of metallic Fe, Ni, and Ni_3Fe (Fig. S5). As discussed above, monometallic Fe/Ni species exhibits worse OER activity than Fe-doped Ni-based catalysts. Therefore, it is reasonably inferred that Ni_3Fe-based active site are the efficient OER center. In addition, the available electrocatalytic active sites were assessed by electrochemically active surface area (ECSA). As exhibited in Figs. S6–S9, $Ni_3Fe_1O_x$@C-800 shows an ECSA of 129.0 cm^{-2}, larger than $Ni_3Fe_1O_x$@C-600 (6.8 cm^{-2}), $Ni_3Fe_1O_x$@C-700 (64.0 cm^{-2}), and $Ni_3Fe_1O_x$@C-900 (53.4 cm^{-2}), indicating more available active sites in the former. Furthermore, charge-transfer ability is one of the main factors that influence electrocatalytic performance of OER. The charge-transfer resistance (R_{ct}) can be derived from the Nyquist plots. As illustrated in Figs. S10–S14, the fitted R_{ct} values for $Ni_3Fe_1O_x$@C-600, $Ni_3Fe_1O_x$@C-700, $Ni_3Fe_1O_x$@C-800, and $Ni_3Fe_1O_x$@C-900 are 39.6, 37.6, 29.6, and 32.8 Ω cm^{-2}. The smaller R_{ct} of $Ni_3Fe_1O_x$@C-800 indicates that the Mott-Schottky interface plays a more favorable role in facilitating charge transfer than those in other $Ni_3Fe_1O_x$@C-T samples [63]. By theoretical calculations, Li et al. found that the theoretical overpotential on Fe site is 0.424 eV, lower than that on Ni site (0.829 eV) in Ni_3Fe-layered double hydroxides [40]. Lin et al. reported that the OER activity would decrease when the Fe element was separated out from the NiFe hydroxide [17]. In addition, Lyu and Nachtigall predicted the lowest theoretical overpotential is 0.4 V on Ni_3Fe nanoparticle encapsulated in a single NC layer [64]. They also found that the OER mechanism was significantly influenced by the charge transfer from Ni_3Fe to NC layers. Therefore, the excellent OER performance of $Ni_3Fe_1O_x$@C-800 should be ascribed to its uniform structure and good charge transfer ability.

The stability of $Ni_3Fe_1O_x$@C-800 was evaluated by supporting it on a graphite plate using the chronoamperometric measurement. As shown in Fig. 5a, negligible change in current density is observed after 12 h, revealing the appreciable durability of the $Ni_3Fe_1O_x$@C-800. The accelerated stability test in the potential range of 1.2–1.65 V for 2000 cycles is displayed in Fig. 5b, where no significant change in current density

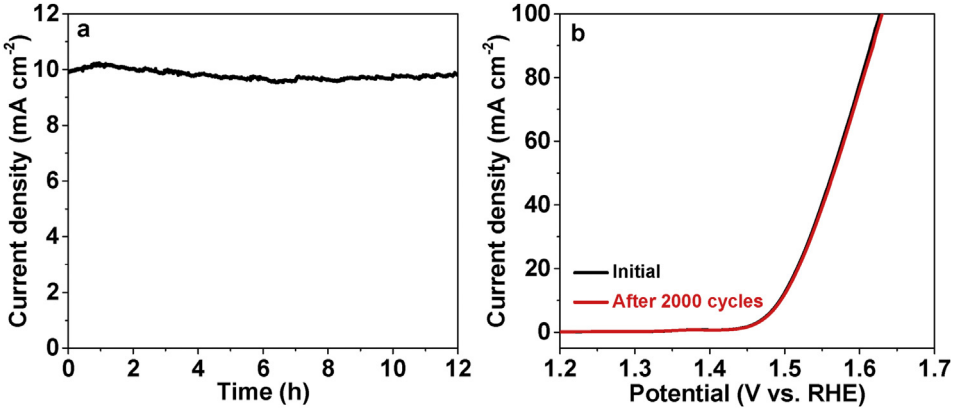

Fig. 5 – (a) Plot of current density versus time for the $Ni_3Fe_1O_x$@C-800. (b) Polarization curves of $Ni_3Fe_1O_x$@C-800 before and after 2000 cycles.

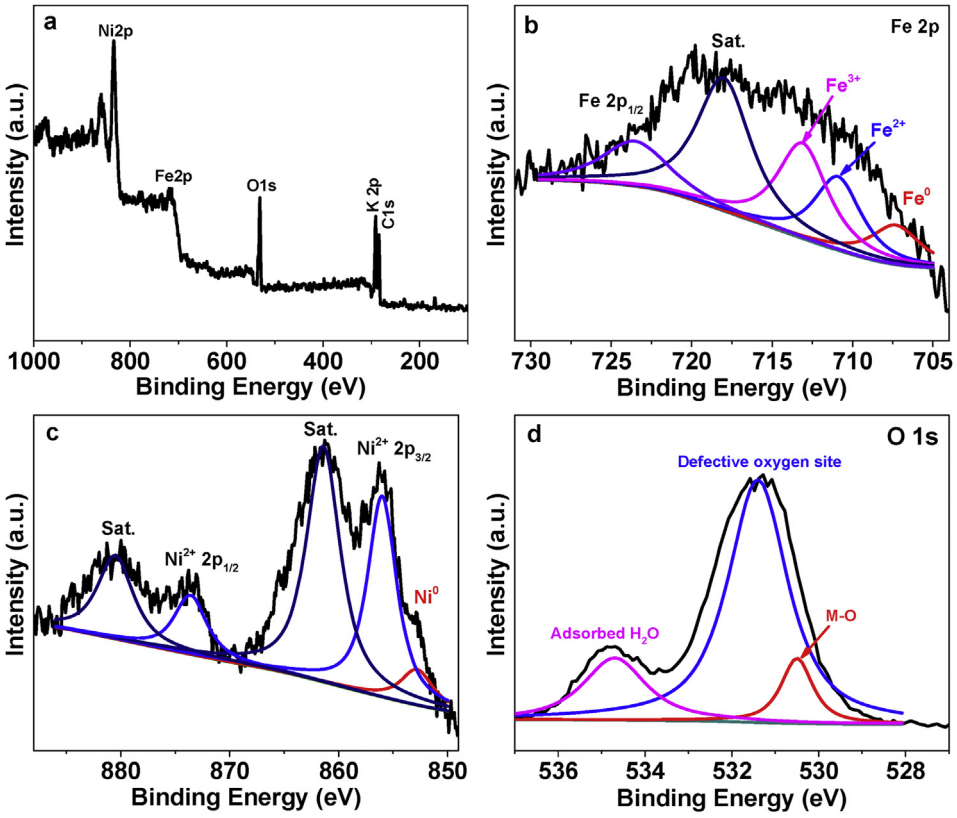

Fig. 6 – XPS survey spectrum (a), and high-resolution XPS spectra of Fe 2p (b), Ni 2p (c), and O 1s (d) of the used $Ni_3Fe_1O_x$@C-800.

profile is observed, signifying outstanding operational stability after the $Ni_3Fe_1O_x$@C-800 is activated. The structure of the electrocatalyst after the durability test was evaluated by XRD and XPS. The XRD presented in Fig. S15 shows that the main species in the $Ni_3Fe_1O_x$@C-800 after OER test is still Ni_3Fe alloy, suggesting its good stability due to the protection of carbon shells. The XPS survey spectrum of the used $Ni_3Fe_1O_x$@C-800 verifies the presence of C, O, Fe, Ni and K (absorbed from the electrolyte) elements (Fig. 6a). After OER electrocatalysis, partial Fe were oxidized to higher valence states, while Fe^0 was still detectable due to the protection of carbon shells (Fig. 6b). Additionally, Ni^0 was still detected in the used $Ni_3Fe_1O_x$@C-800 due to the wrapping of amorphous carbon shells (Fig. 6c). In addition, compared with the fresh $Ni_3Fe_1O_x$@C-800, the relative content of defective oxygen sites in the used $Ni_3Fe_1O_x$@C-800 increased (Fig. 6d), indicating that surface oxygen species took part in the OER. Combining with the XRD, XPS and electrochemical analysis, we can infer that surface oxidized Fe/Ni species are responsible for electrocatalytic water oxidation, while the Ni_3Fe core favors the electron and charge transfer.

Conclusions

In the present work, we have synthesized a Ni_3Fe alloy wrapped by amorphous carbon shells via a simple annealing process. The Ni_3Fe_1-TA annealed at 800 °C offers the best OER activity due to the presence of more active sites, smaller charge transfer, and better intrinsic activity. As a result, the $Ni_3Fe_1O_x$@C-800 exhibits low overpotential (η_{10}) of 264 mV, small Tafel slope of 68 mV dec^{-1}, and good stability in alkaline media. Compared with monometallic FeO_x@C-800 and NiO_x@C-800, bimetallic $Ni_3Fe_1O_x$@C-800 shows lower OER barrier (ca. 324 kJ mol^{-1}) due to a cooperative catalytic mechanism between Fe and Ni sites in facilitating OER electrocatalysis.

Declaration of competing interest

The authors declare that they have no known competing financial interests or personal relationships that could have appeared to influence the work reported in this paper.

Acknowledgments

This work was supported by the National Natural Science Foundation of China (22075099), Natural Science Foundation of Jilin Province (20180101291JC).

Appendix A. Supplementary data

Supplementary data to this article can be found online at https://doi.org/10.1016/j.ijhydene.2021.10.119.

REFERENCES

[1] Radwan A, Jin H, He D, Mu S. Design engineering, synthesis protocols, and energy applications of MOF-derived electrocatalysts. Nano-Micro Lett 2021;13:132.
[2] Yu Z-Y, Duan Y, Feng X-Y, Yu X, Gao M-R, Yu S-H. Clean and affordable hydrogen fuel from alkaline water splitting: past, recent progress, and future prospects. Adv Mater 2021;33:2007100.
[3] Zhao R, Li Q, Jiang X, Huang S, Fu G, Lee J-M. Interface engineering in transition metal-based heterostructures for oxygen electrocatalysis. Mater Chem Front 2021;5:1033–59.
[4] Liang J, Liu Q, Li T, Luo Y, Lu S, Shi X, et al. Magnetron sputtering enabled sustainable synthesis of nanomaterials for energy electrocatalysis. Green Chem 2021;23:2834–67.
[5] Li X, Zhao H, Liang J, Luo Y, Chen G, Shi X, et al. A-site perovskite oxides: an emerging functional material for electrocatalysis and photocatalysis. J Mater Chem 2021;9:6650–70.
[6] Zhao C-X, Liu J-N, Wang J, Ren D, Li B-Q, Zhang Q. Recent advances of noble-metal-free bifunctional oxygen reduction and evolution electrocatalysts. Chem Soc Rev 2021;50:7745–78.
[7] Gao J, Tao H, Liu B. Progress of nonprecious-metal-based electrocatalysts for oxygen evolution in acidic media. Adv Mater 2021:2003786.
[8] Li L, Wang P, Shao Q, Huang X. Recent progress in advanced electrocatalyst design for acidic oxygen evolution reaction. Adv Mater 2021:2004243.
[9] Cao Y, Wang T, Li X, Zhang L, Luo Y, Zhang F, et al. A hierarchical CuO@NiCo layered double hydroxide core-shell nanoarray as an efficient electrocatalyst for the oxygen evolution reaction. Inorg Chem Front 2021;8:3049–54.
[10] Vij V, Sultan S, Harzandi AM, Meena A, Tiwari JN, Lee W-G, et al. Nickel-based electrocatalysts for energy-related applications: oxygen reduction, oxygen evolution, and hydrogen evolution reactions. ACS Catal 2017;7:7196–225.
[11] Zhao J, Zhang J-J, Li Z-Y, Bu X-H. Recent progress on NiFe-based electrocatalysts for the oxygen evolution reaction. Small 2020;16:2003916.
[12] Ye C, Zhang L, Yue L, Deng B, Cao Y, Liu Q, et al. A NiCo LDH nanosheet array on graphite felt: an efficient 3D electrocatalyst for the oxygen evolution reaction in alkaline media. Inorg Chem Front 2021;8:3162–6.
[13] Meng C, Cao Y, Luo Y, Zhang F, Kong Q, Alshehri AA, et al. A Ni-MOF nanosheet array for efficient oxygen evolution electrocatalysis in alkaline media. Inorg Chem Front 2021;8:3007–11.
[14] Chen Y, Rui K, Zhu J, Dou SX, Sun W. Recent progress on nickel-based oxide/(oxy)hydroxide electrocatalysts for the oxygen evolution reaction. Chem Eur J 2019;25:703–13.
[15] Li Y, Bao X, Chen D, Wang Z, Dewangan N, Li M, et al. A minireview on nickel-based heterogeneous electrocatalysts for water splitting. ChemCatChem 2019;11:5913–28.
[16] Zhang W, Li D, Zhang L, She X, Yang D. NiFe-based nanostructures on nickel foam as highly efficiently electrocatalysts for oxygen and hydrogen evolution reactions. J Energy Chem 2019;39:39–53.
[17] Kuai C, Xu Z, Xi C, Hu A, Yang Z, Zhang Y, et al. Phase segregation reversibility in mixed-metal hydroxide water oxidation catalysts. Nat Catal 2020;3:743–53.
[18] Lee S, Bai L, Hu X. Deciphering iron-dependent activity in oxygen evolution catalyzed by nickel-iron layered double hydroxide. Angew Chem Int Ed 2020;59:8072–7.
[19] Zhang J, Yu L, Chen Y, Lu XF, Gao S, Lou XW. Designed formation of double-shelled Ni-Fe layered-double-hydroxide nanocages for efficient oxygen evolution reaction. Adv Mater 2020;32:1906432.
[20] Wu Z, Zou Z, Huang J, Gao F. Fe-doped NiO mesoporous nanosheets array for highly efficient overall water splitting. J Catal 2018;358:243–52.
[21] Li Y, Lu M, Wu Y, Ji Q, Xu H, Gao J, et al. Morphology regulation of metal-organic framework-derived nanostructures for efficient oxygen evolution electrocatalysis. J Mater Chem 2020;8:18215–9.
[22] Gong M, Li Y, Wang H, Liang Y, Wu JZ, Zhou J, et al. An advanced Ni-Fe layered double hydroxide electrocatalyst for water oxidation. J Am Chem Soc 2013;135:8452–5.
[23] Ma W, Ma R, Wang C, Liang J, Liu X, Zhou K, et al. A superlattice of alternately stacked Ni-Fe hydroxide nanosheets and graphene for efficient splitting of water. ACS Nano 2015;9:1977–84.
[24] Chen C, Tuo Y, Lu Q, Lu H, Zhang S, Zhou Y, et al. Hierarchical trimetallic Co-Ni-Fe oxides derived from core-shell structured metal-organic frameworks for highly efficient oxygen evolution reaction. Appl Catal, B 2021;287:119953.
[25] Cui X, Zhang B, Zeng C, Wen H, Guo S. Monolithic nanoporous Ni-Fe alloy by dealloying laser processed Ni-Fe-Al as electrocatalyst toward oxygen evolution reaction. Int J Hydrogen Energy 2018;43:15234–44.
[26] Kim J-H, Youn DH, Kawashima K, Lin J, Lim H, Mullins CB. An active nanoporous Ni(Fe) OER electrocatalyst via selective dissolution of Cd in alkaline media. Appl Catal, B 2018;225:1–7.
[27] Wang B, Zhao K, Yu Z, Sun C, Wang Z, Feng N, et al. In situ structural evolution of the multi-site alloy electrocatalyst to manipulate the intermediate for enhanced water oxidation reaction. Energy Environ Sci 2020;13:2200–8.
[28] Zhang B, Wang L, Cao Z, Kozlov SM, Garcia de Arquer FP, Dinh CT, et al. High-valence metals improve oxygen evolution reaction performance by modulating 3dmetal oxidation cycle energetics. Nat Catal 2020;3:985–92.
[29] Chen Q-Q, Hou C-C, Wang C-J, Yang X, Shi R, Chen Y. Ir4+-Doped NiFe LDH to expedite hydrogen evolution kinetics as a Pt-like electrocatalyst for water splitting. Chem Commun 2018;54:6400–3.
[30] Liu Z, Tan H, Xin J, Duan J, Su X, Hao P, et al. Metallic intermediate phase inducing morphological transformation in thermal nitridation: Ni3FeN-based three-dimensional hierarchical electrocatalyst for water splitting. ACS Appl Mater Interfaces 2018;10:3699–706.
[31] Xuan C, Wang J, Xia W, Zhu J, Peng Z, Xia K, et al. Heteroatom (P, B, or S) incorporated NiFe-based nanocubes as efficient electrocatalysts for the oxygen evolution reaction. J Mater Chem 2018;6:7062–9.
[32] Xuan C, Xia K, Lei W, Xia W, Xiao W, Chen L, et al. Composition-dependent electrocatalytic activities of NiFe-based selenides for the oxygen evolution reaction. Electrochim Acta 2018;291:64–72.
[33] Xu D, Stevens MB, Rui Y, DeLuca G, Boettcher SW, Reichmanis E, et al. The role of Cr doping in Ni-Fe oxide/(oxy) hydroxide electrocatalysts for oxygen evolution. Electrochim Acta 2018;265:10–8.
[34] Cheng W, Zhao X, Su H, Tang F, Che W, Zhang H, et al. Lattice-strained metal–organic-framework arrays for bifunctional oxygen electrocatalysis. Nat Energy 2019;4:115–22.
[35] Gong L, Yang H, Douka AI, Yan Y, Xia BY. Recent progress on NiFe-based electrocatalysts for alkaline oxygen evolution. Adv Sustainable Syst 2021;5:2000136.
[36] Deng C, Wu KH, Scott J, Zhu S, Amal R, Wang DW. Core/shell NiFe nanoalloy with a discrete N-doped graphitic carbon

cover for enhanced water oxidation. ChemElectroChem 2018;5:732–6.
[37] Tu Y, Ren P, Deng D, Bao X. Structural and electronic optimization of graphene encapsulating binary metal for highly efficient water oxidation. Nanomater Energy 2018;52:494–500.
[38] Gong H, Zheng X, Zeng K, Yang B, Liang X, Li L, et al. Ni3Fe nanoalloys embedded in N-doped carbon derived from dual-metal ZIF: efficient bifunctional electrocatalyst for Zn-air battery. Carbon 2021;174:475–83.
[39] Adegbemiga YB, Ullah N, Xie M, Hussain S, Oluigbo CJ, Yaseen W, et al. Ni3Fe nanoparticles enclosed by B-doped carbon for efficient bifunctional performances of oxygen and hydrogen evolution reactions. J Alloys Compd 2020;835:155267.
[40] Zhao X, Xiong X, Duan X, Xu Y, Li Y. First-principles study of oxygen evolution reaction on Ni3Fe-layered double hydroxides surface with different oxygen coverage. Mol Catal 2020;490:110957.
[41] Jin H, Mao S, Zhan G, Xu F, Bao X, Wang Y. Fe incorporated alpha-Co(OH)(2) nanosheets with remarkably improved activity towards the oxygen evolution reaction. J Mater Chem 2017;5:1078–84.
[42] Yang J, Wang X, Li B, Ma L, Shi L, Xiong Y, et al. Novel iron/cobalt-containing polypyrrole hydrogel-derived trifunctional electrocatalyst for self-powered overall water splitting. Adv Funct Mater 2017;27:1606497.
[43] Wu Z, Wang X, Huang J, Gao F. A Co-doped Ni-Fe mixed oxide mesoporous nanosheet array with low overpotential and high stability towards overall water splitting. J Mater Chem 2018;6:167–78.
[44] Wang A-L, Xu H, Li G-R. NiCoFe layered triple hydroxides with porous structures as high-performance electrocatalysts for overall water splitting. ACS Energy Lett 2016;1:445–53.
[45] Liu N, Guan J. Core–shell Co3O4@ FeOx catalysts for efficient oxygen evolution reaction. Mater Today Energy 2021;21:100715.
[46] Lin Y, Wan H, Wu D, Chen G, Zhang N, Liu X, et al. Metal-organic framework hexagonal nanoplates: bottom-up synthesis, topotactic transformation, and efficient oxygen evolution reaction. J Am Chem Soc 2020;142:7317–21.
[47] Qiu H-J, Du P, Hu K, Gao J, Li H, Liu P, et al. Metal and nonmetal codoped 3D nanoporous graphene for efficient bifunctional electrocatalysis and rechargeable zn–air batteries. Adv Mater 2019;31:1900843.
[48] Dong C, Yuan X, Wang X, Liu X, Dong W, Wang R, et al. Rational design of cobalt-chromium layered double hydroxide as a highly efficient electrocatalyst for water oxidation. J Mater Chem 2016;4:11292–8.
[49] Zhang Q, Liu N, Guan J. Charge-transfer effects in Fe-Co and Fe-Co-Y oxides for electrocatalytic water oxidation reaction. ACS Appl Energy Mater 2019;2:8903–11.
[50] Liu N, Zhang Q, Guan J. A binuclear Co-based metal-organic framework towards efficient oxygen evolution reaction. Chem Commun 2021;57:5016–9.
[51] Wang Q, Liu Z, Zhao H, Huang H, Jiao H, Du Y. MOF-derived porous Ni2P nanosheets as novel bifunctional electrocatalysts for the hydrogen and oxygen evolution reactions. J Mater Chem 2018;6:18720–7.
[52] Gao Z, Yu ZW, Liu FQ, Yu Y, Su XM, Wang L, et al. Ultralow-content iron-decorated Ni-MOF-74 fabricated by a metal-organic framework surface reaction for efficient electrocatalytic water oxidation. Inorg Chem 2019;58:11500–7.
[53] Li J, Huang W, Wang M, Xi S, Meng J, Zhao K, et al. Low-crystalline bimetallic metal-organic framework electrocatalysts with rich active sites for oxygen evolution. ACS Energy Lett 2019;4:285–92.
[54] Senthil Raja D, Chuah X-F, Lu S-Y. In situ grown bimetallic MOF-based composite as highly efficient bifunctional electrocatalyst for overall water splitting with ultrastability at high current densities. Adv Energy Mater 2018;8:1801065.
[55] Ke W, Zhang Y, Imbault AL, Li Y. Metal-organic framework derived iron-nickel sulfide nanorods for oxygen evolution reaction. Int J Hydrogen Energy 2021;46:20941–9.
[56] Rui K, Zhao G, Chen Y, Lin Y, Zhou Q, Chen J, et al. Hybrid 2D dual-metal-organic frameworks for enhanced water oxidation catalysis. Adv Funct Mater 2018;28:1801554.
[57] Zhao J, Zhang X, Liu M, Jiang Y-Z, Wang M, Li Z-Y, et al. Metal-organic-framework-derived porous 3D heterogeneous NiFex/NiFe2O4@NC nanoflowers as highly stable and efficient electrocatalysts for the oxygen-evolution reaction. J Mater Chem 2019;7:21338–48.
[58] Li X, Fan M, Wei D, Wang X, Wang Y. Core-shell NiO/C@NiFe-LDH nanocomposite as an efficient electrocatalyst for oxygen evolution reaction. J Electrochem Soc 2020;167:024501.
[59] Zhao S, Li M, Han M, Xu D, Yang J, Lin Y, et al. Defect-rich Ni3FeN nanocrystals anchored on N-doped graphene for enhanced electrocatalytic oxygen evolution. Adv Funct Mater 2018;28:1706018.
[60] Yuan J-T, Hou J-J, Liu X-L, Feng Y-R, Zhang X-M. Optimized trimetallic benzotriazole-5-carboxylate MOFs with coordinately unsaturated active sites as an efficient electrocatalyst for the oxygen evolution reaction. Dalton Trans 2020;49:750–6.
[61] Wang M, Dong C-L, Huang Y-C, Li Y, Shen S. Electronic structure evolution in tricomponent metal phosphides with reduced activation energy for efficient electrocatalytic oxygen evolution. Small 2018;14:1801756.
[62] Chung DY, Lopes PP, Martins PFBD, He H, Kawaguchi T, Zapol P, et al. Dynamic stability of active sites in hydr(oxy) oxides for the oxygen evolution reaction. Nat Energy 2020;5:222–30.
[63] Tan Y, Liu P, Chen L, Cong W, Ito Y, Han J, et al. Monolayer MoS2 films supported by 3D nanoporous metals for high-efficiency electrocatalytic hydrogen production. Adv Mater 2014;26:8023–8.
[64] Lyu P, Nachtigall P. Systematic computational investigation of an Ni3Fe catalyst for the OER. Catal Today 2020;345:220–6.